The PSF of spiral CT

Gil Schwarzband and Nahum Kiryati

School of Electrical Engineering, Tel Aviv University, Ramat Aviv 69978, Israel

E-mail: gelik@post.tau.ac.il, nk@eng.tau.ac.il

Abstract. CT scanners are usually described by their in-plane resolution and slice-sensitivity profile (SSP). Other imaging systems are characterized by their point spread function (PSF). The PSF is an excellent basis for the analysis, design and enhancement of imaging systems. The 3D PSF of CT systems has rarely been considered, and has usually been approximated by a 3D Gaussian. We present mathematical analysis of the PSF of single-slice and multi-slice fan-beam and cone-beam CT, for major reconstruction algorithms. We show that the PSF has a complicated, non-separable 3D shape. It is anisotropic in the xy plane and twisted in the z direction. Furthermore, the PSF is space variant in all three axes. In particular, it rotates as the input impulse function moves in the z direction. The PSF may also have effective discontinuities, that can lead to streaking artifacts. Indirect measurements of the PSF can be misleading. We support the theoretical results by direct experimental measurements of the PSF.

Submitted to: *Physics in Medicine and Biology*

1. Introduction

Spiral and multi-slice spiral X-Ray computed tomography (CT) are well-established techniques. They have effectively replaced classical planar slice-by-slice scanning: all scanners in clinical use are nowadays spiral.

The point spread function (PSF) is the fundamental characteristic of any linear imaging system. However, following the legacy of classical CT, spiral CT systems are commonly characterized by their in-plane (xy) resolution and by their slice sensitivity profile (SSP) along the z axis. Analytical and experimental analysis of the SSP was carried out by Wang and Vannier (1994a,b), Wang *et al* (1994), Polacin *et al* (1993), Hu and Fox (1996) and Hsieh (2003). The PSF of spiral CT systems has hardly been studied and is rarely mentioned in the literature.

Experimental measurements of the PSF of CT systems were reported by Wang *et al* (1998) and Chen and Ning (2004). They obtained step response measurements at the boundary of a relatively large body, and used them to compute the PSF. It was concluded that the PSF can be approximated by a 3-D Gaussian. However, this indirect approach relies on the assumptions that the PSF is space-invariant (at least locally) and

separable. As we will show, both assumptions do not generally hold. Interesting space-variant phenomena, that we shall discuss, could have been averaged out, leading to the apparent Gaussian.

The major novel contribution of this study is the derivation of the PSF of single-slice and multi-slice spiral CT systems. We show that the PSF has the following surprising and important properties:

- The PSF has a complicated 3-D shape, twisted along the z-axis.
- The PSF is not isotropic in the xy plane and leads to anisotropic blur.
- The PSF is highly space-variant in the z direction. In particular, it rotates as a function of the z position of the input impulse, following the rotation of the x-ray source.
- The PSF has some spatial variance also in the xy plane.
- The PSF may have discontinuities, that can lead to visible streak artifacts.

The first three properties have not been previously discussed. The possibility that PSF can be space-variant in z axis has been indicated in several works (Wang *et al* 1994, Yen *et al* 1999a,b, La Rivière and Pan 2002a,b), but this variance was treated merely as "longitudinal aliasing effect" and no analysis was given. All other works that deal with space-variance of the PSF discuss only the variance in the xy plane.

In this work we analytically derive expressions for the PSF, for all major fan-beam reconstruction algorithms and the ASSR cone-beam reconstruction algorithm. They can be readily adapted to obtain the PSF of any particular CT scanner/collimation. We show the shape of the PSF for typical cases.

Some properties of the PSF that are discussed here manifest themselves indirectly in experimental results reported by Polacin *et al* (1993), La Rivière and Pan (2002a), Yen *et al* (1999b) and Fleischmann *et al* (2000). We support our results by direct experimental measurements of the PSF.

The paper is organized as follows. Section 2 provides an overview of various CT geometries and reconstruction techniques, and establishes a mathematical framework that describes an acquisition-reconstruction process in single-slice and multi-slice fan-beam CT. Section 3 analytically derives the PSF for several typical cases. Section 4 presents experimental results. The conclusions are summarized in section 5.

2. CT geometries and reconstruction algorithms

This section presents mathematical models for the acquisition-reconstruction processes in different spiral X-ray CT configurations. We start our discussion with legacy fan-beam geometries and reconstruction algorithms that were in wide clinical use up to the end of the 1990s. This discussion is based on Jain (1989), Crawford and King (1990), Dawson and Lees (2001) and Schaller *et al* (2000). This is necessary in order to understand the deep roots of the PSF properties mentioned above, which appear to be common to all geometries. Then we proceed to discuss the modern cone-beam geometry.

2.1. Spiral parallel-beam geometry

Although spiral CT systems are either fan-beam or cone-beam, it is beneficial to start our discussion with a simplified theoretic model using parallel-beam geometry.

In *planar* parallel-beam geometry each projection ray is defined by the inclination θ of the detectors, and the position s on the linear detector array. The projection $g(s,\theta)$ of an object slice $f(x,y)$ is given by the Radon transform

$$g(s,\theta) = \iint_{-\infty}^{\infty} \delta(x\cos\theta + y\sin\theta - s) f(x,y) dxdy \ , \tag{1}$$

where $\theta \in [-\pi/2, \pi/2)$ for halfscan acquisition.

Our discussion here and in the sequel is in the continuous domain. That is, we do not consider discretization effects caused by sampling of s and θ. These effects should not be different in spiral CT than in classical planar CT, and have been studied extensively in the past (see, for example, Rattey and Lindgren 1981). We are interested in longitudinal discretization effects specific to the spiral CT.

In *spiral (helical)* CT, the reference position z_0 of the patient table and the angle τ of the detectors both increase at a constant rate. Thus,

$$z_0 = v\tau \ . \tag{2}$$

This is effectively equivalent to helical movement of the source and detectors around and along the patient.

We denote the spiral projection set obtained from an object $f(x,y,z)$ by $g(s,\tau)$, where τ grows by 2π per revolution. Then, as in (1),

$$g(s,\tau) = \iint_{-\infty}^{\infty} \delta(x\cos\tau + y\sin\tau - s) \int_{-\infty}^{\infty} A(z - v\tau) f(x,y,z) dzdxdy, \tag{3}$$

where $A(\Delta z)$ is the axial aperture of the detector. $A(\Delta z)$ is approximated by a rectangular function defined by the width d of the detector. An important characteristic of the setup is the spiral pitch $p = 2\pi v/d$. Typically $1 \le p \le 2$.

Most reconstruction methods define "reconstruction planes". For a reconstruction plane $z = z_0$, they estimate from the dataset $g(s,\tau)$ the conventional *planar* parallel-beam halfscan sinogram $\bar{g}(s,\theta)$ that would be obtained if a planar scan was performed at $z = z_0$. This is done by weighting data from two or more nearby spiral turns:

$$\bar{g}(s,\theta,z) = \sum_{k=-\infty}^{\infty} g((-1)^k s, \theta + k\pi) \cdot w(v\cdot(\theta + k\pi) - z) \ , \tag{4}$$

where $w(\Delta z)$ is a weighting function, and $\Delta z = v\cdot(\theta + k\pi) - z$ is the displacement between the reconstruction plane and the ray being weighted. Common reconstruction methods differ only in w. In particular, two basic reconstruction methods are called 180LI are 360LI, meaning 180 and 360 degrees linear interpolation. The function w for these methods is triangular, with support $(-pd/2, pd/2)$ and $(-pd, pd)$ respectively.

Reconstruction is via the back-projection approximation

$$b(r,\varphi,z) = \int_{-\pi/2}^{\pi/2} g(r\cos(\theta - \varphi), \theta) d\theta \tag{5}$$

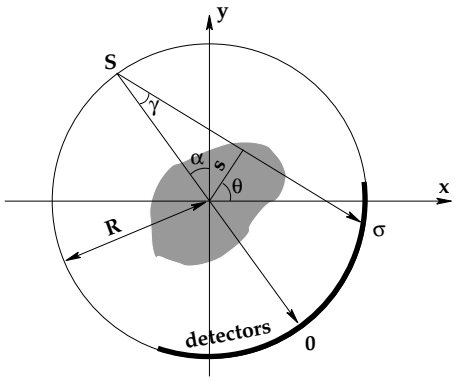

Figure 1. Planar fan-beam geometry.

of $f(x, y, z)$, followed by convolution with a deblurring filter h. Thus, $\tilde{f} = b * h$.

2.2. Multi-slice spiral parallel-beam geometry

In multi-slice (multidetector) spiral CT, the detector array consists of several parallel adjacent detector rows. This allows faster table movement and faster data acquisition (Dawson and Lees 2001, Schaller *et al* 2000). Consider for simplicity *parallel-beam* multidetector spiral geometry. Let N be the number of parallel detector rows and n the detector row index. Then $\bar{n} = (N + 1)/2$ is the average of the indices of the N slices. If the center of the detector array is at $z_c = v\tau$, the position of a specific detector is $z_n = v\tau + (n - \bar{n})d$. Thus, the projection set $g_n(s, \tau)$ obtained by detector n is

$$g_n(s,\tau) = \iint_{-\infty}^{\infty} \delta(x\cos\tau + y\sin\tau - s) \int_{-\infty}^{\infty} A(z - v\tau - (n-\bar{n})d) f(x,y,z)\,dz\,dx\,dy \ . \quad (6)$$

Compare to equation 3.

The reconstruction principle is similar to the single-slice case. The estimated sinogram $\bar{g}(s, \theta, z)$ is the superposition

$$\bar{g}(s,\theta,z) = \sum_n \bar{g}_n(s,\theta,z) \quad (7)$$

of individual detector contributions $\bar{g}_n(s, \theta, z)$, given by

$$\bar{g}_n(s,\theta,z) = \sum_{k=-\infty}^{\infty} g((-1)^k s, \theta + k\pi) \cdot w_n(v \cdot (\theta + k\pi) + (n - \bar{n})d - z) \ . \quad (8)$$

Compare to equation 4.

2.3. Planar fan-beam geometry

In fan-beam geometry, the beam is emitted by a point-source S. Its position is characterized by the angle α, as shown in figure 1. Each projected ray is represented by the parameters (α, γ), where γ is the angular deviation of the ray with respect to

the central direction SO of the beam. Every ray (α, γ) in fan-beam geometry coincides with a ray in parallel-beam geometry, with parameters (s, θ) given by

$$s = R\sin\gamma \qquad \theta = [\alpha+\gamma]^{\pi}_{-\pi} \quad , \tag{9}$$

where $-\gamma_{max} \leq \gamma \leq \gamma_{max}$ and

$$[x]^{\pi}_{-\pi} \equiv ((x+\pi) \bmod 2\pi) - \pi. \tag{10}$$

The halfscan sinogram of $f(x, y)$ is

$$g_{\text{fan}}(\alpha,\gamma) = \iint_{-\infty}^{\infty} \delta(x\cos(\gamma+\alpha)+y\sin(\gamma+\alpha)-R\sin\gamma) f(x,y)dxdy, \tag{11}$$

where α is in the range $[-\pi/2-\gamma_{max}, \pi/2+\gamma_{max})$. So, a halfscan parallel-beam sinogram can be obtained from the original fan-beam one by

$$g(s,\theta) = g_{\text{fan}}(\theta - \arcsin\frac{s}{R}, \arcsin\frac{s}{R}) \ . \tag{12}$$

Conventional parallel-beam reconstruction can then be carried out.

2.4. Spiral fan-beam geometry

In fan-beam spiral geometry, we denote the projection set obtained from an object $f(x, y, z)$ as $g_{\text{fan}}(\beta, \gamma)$. The angle β grows by 2π with each rotation. The position of the detectors can thus be expressed as $z_0 = v\beta$. The dataset obtained is

$$\begin{aligned} g_{\text{fan}}(\beta,\gamma) = &\iint_{-\infty}^{\infty} \delta(x\cos(\gamma+\beta)+y\sin(\gamma+\beta)-R\sin\gamma) \\ &\cdot \int_{-\infty}^{\infty} A(z-v\beta) f(x,y,z)dzdxdy \ . \end{aligned} \tag{13}$$

As in the spiral parallel-beam case, spiral fan-beam reconstruction begins with estimation, for each z, of the dataset $\bar{g}_{\text{fan}}(\alpha, \gamma, z)$ by interpolation (weighting) of data from nearby spiral turns. Here, the weight depends on $\Delta\beta$ and γ: $w(\Delta\beta, \gamma)$. Thus, the estimated dataset is

$$\bar{g}_{\text{fan}}(\alpha,\gamma,z) = \sum_{k=-\infty}^{\infty} g_{\text{fan}}(\alpha+2k\pi,\gamma) \cdot w(\alpha+2k\pi-\frac{z}{v},\gamma) \ . \tag{14}$$

Here $\alpha \in [-\pi, \pi)$. Various weighting functions have been proposed, see e.g. Crawford and King (1990), Schaller *et al* (2000). A popular one is CSH-HH (Crawford and King 1990), the fan-beam version of 180LI interpolation:

$$w(\Delta\beta,\gamma) = \begin{cases} \frac{\pi+\Delta\beta+2\gamma}{\pi+2\gamma} & -\pi-2\gamma \leq \Delta\beta < 0 \\ \frac{\pi-\Delta\beta-2\gamma}{\pi-2\gamma} & 0 \leq \Delta\beta < \pi-2\gamma \\ 0 & \text{otherwise} \end{cases} \tag{15}$$

The next step is to derive a parallel-beam halfscan dataset from the estimated fan-beam fullscan dataset. In this geometry, the ray opposite to (α, γ) is $([\alpha+\pi+2\gamma]^{\pi}_{-\pi}, -\gamma)$. Thus,

$$\begin{aligned} \bar{g}(s,\theta,z) = &\bar{g}_{\text{fan}}(\theta - \arcsin\frac{s}{R}, \arcsin\frac{s}{R}, z) \\ &+\bar{g}_{\text{fan}}([\theta+\arcsin\frac{s}{R}+\pi]^{\pi}_{-\pi}, -\arcsin\frac{s}{R}, z) \ , \end{aligned} \tag{16}$$

where $\theta \in [-\pi/2, \pi/2)$. Backprojection and filtering complete the reconstruction.

The mathematical model for acquisition and reconstruction with *multi-slice* fan-beam geometry is a straightforward combination of the above expressions for the multi-slice parallel-beam and single-slice fan-beam configurations. It is omitted for brevity.

2.5. Multi-slice spiral cone-beam

In our modelling of multi-slice spiral geometry, we neglected the fact that the rays diverge not only in the xy plane (forming a fan-beam), but also in the z direction, forming a *c*one-beam. This approximation is valid only for systems with up to four slices (Schaller *et al* 2000, Dawson and Lees 2001). To deal with the general geometry, cone-beam reconstruction algorithms have been developed.

As a matter of fact, there are dozens of different spiral cone-beam reconstruction algorithms. Two noticeable groups are the "approximate" and "exact" algorithms (see the contemporary overview and definitions in Wang and Lee 2003). Among approximate algorithms we shall note SSR (Noo *et al* 1999), ASSR (Kachelrieß *et al* 2000), AMPR (Flohr *et al* 2003) and SMPR (Stierstorfer *et al* 2002). Exact algorithms were developed by Grangeat (1991), Katsevich (2002 and 2004), Noo and Heuscher (2002), Zou and Pan (2004) and many others.

In spite of the rapidly growing interest in the practical implementation of the exact reconstruction algorithms, there is no evidence that they are widely used in clinical CT scanners. On the contrary, the above-mentioned approximate algorithms, most of them co-authored by researchers affiliated with CT manufacturers, seem to dominate. This is also noticed in Wang and Lee (2003) and in other overviews. We therefore limit our discussion below to the ASSR algorithm, which is a basic and practical representative of the approximate algorithms group. The reader is referred to Kachelrieß *et al* (2000) for the description of this algorithm. In section 3.6 we will analyze the PSF of the ASSR algorithm and discuss a generalization of this result to a wide range of other algorithms.

3. Calculation of the PSF

In this section we derive the PSF of single-slice and multi-slice CT for typical setups, using the analytical models developed in section 2. The derivation can be readily extended to other specific CT setups.

For simplicity we start our analysis with the purely theoretical *parallel-beam* geometry. Then we extend our model to the practical *fan-beam* geometry. Throughout our analysis of fan-beam geometry we neglect the divergence of the rays in the z direction (cone-beam effect). This assumption is common in the analysis of CT systems with up to four slices (Schaller *et al* 2000, Dawson and Lees 2001). It is based on the observation that the region of interest (patient's radius) is much smaller than the X-ray gantry rotation radius, so that the rays do not diverge much in the z direction while passing through the region of interest. Thus, for scanners with up to four slices, the cone-beam

effect has little influence on the PSF. In particular, it has no influence at all on the PSF at the isocenter. Finally, we consider the cone-beam geometry and the corresponding reconstruction algorithms.

Lemma: Given a separable halfscan sinogram of the form

$$g(s,\theta) = \delta(x_0\cos\theta + y_0\sin\theta - s)g(\theta)\ , \tag{17}$$

the backprojection is

$$b(r',\varphi') = \begin{cases} \frac{1}{r'}g(\varphi'+\frac{\pi}{2}) & -\pi \le \varphi' < 0 \\ \frac{1}{r'}g(\varphi'-\frac{\pi}{2}) & 0 \le \varphi' < \pi \end{cases} \tag{18}$$

where (r',φ') are polar coordinates with the origin at (x_0,y_0), so that $x-x_0 = r'\cos\varphi'$ and $y-y_0 = r'\sin\varphi'$.
Proof is straightforward and is omitted for brevity.

3.1. Single-slice parallel-beam spiral CT

Consider a single-slice parallel-beam spiral CT system with pitch 2. Let us find its response to an impulse located at $z=0$: $f(x,y,z) = \delta(x-x_0, y-y_0, z)$.

For pitch $p=2$, the speed v is d/π. Using (3) we obtain

$$g(s,\tau) = \begin{cases} \delta(x_0\cos\tau + y_0\sin\tau - s) & -\pi/2 \le \tau < \pi/2 \\ 0 & \text{otherwise} \end{cases} \tag{19}$$

We now use (4) to estimate the effective halfscan sinograms $\bar{g}(s,\theta,z)$ for $\theta \in [-\pi/2, \pi/2)$. Note that because $g(s,\tau)$ is non-zero also only for $-\pi/2 \le \tau < \pi/2$, the only relevant term in (4) is the one with $k=0$:

$$\bar{g}(s,\theta,z) = g(s,\theta)w(v\theta - z) = \delta(x_0\cos\theta + y_0\sin\theta - s)w(d\frac{\theta}{\pi} - z)\ . \tag{20}$$

According to the lemma, the back-projection of (20) is

$$b(r',\varphi',z) = \frac{1}{r'}\begin{cases} w((\frac{\varphi'}{\pi}+\frac{1}{2})d - z) & -\pi \le \varphi' < 0 \\ w((\frac{\varphi'}{\pi}-\frac{1}{2})d - z) & 0 \le \varphi' < \pi \end{cases} \tag{21}$$

in cylindrical coordinates centered at $(x_0, y_0, 0)$.

Equation (21) is an analytic expression for the 3-D PSF of a general parallel-beam single-slice spiral CT system with pitch 2, without the final deblurring step. Specifically for 180LI reconstruction, we substitute for w a triangular function supported on $(-d,d)$. Here and in the sequel, following backprojection, we applied the Generalized Hamming filter (Jain 1989, p. 442, $\alpha = 0.4$). The 3-D shape of the PSF (21) is shown in figure 2 (left) by its sections at $z \in \{0, \frac{1}{4}d, \frac{1}{2}d, \frac{3}{4}d, d\}$. For $z \ge 1\frac{1}{2}d$ the PSF vanishes. For $z<0$ the result is similar, but antisymmetric.

It must be emphasized that the PSF is highly variant to shift of the input delta function in z. One can verify by substituting $f = \delta(x-x_0, y-y_0, z-z_0)$ as input, that the PSF shown above rotates by z_0/v radians around z axis. That is, the orientation of the PSF follows the direction of the beam at the moment when source-detector system passes by the delta function at $z=z_0$.

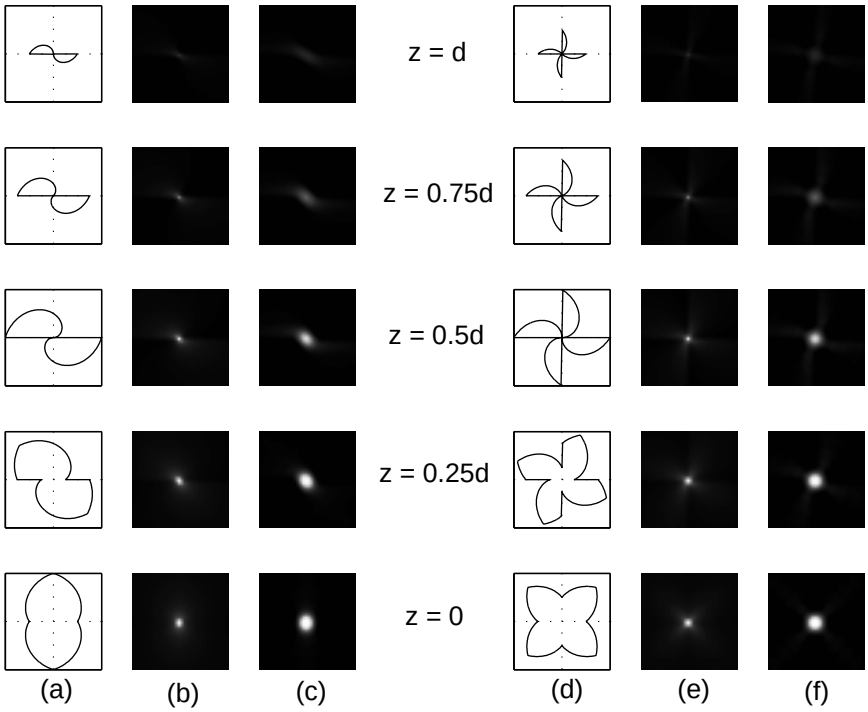

Figure 2. Sections through the computed PSF of single-slice (*left*) and two-slice (*right*) spiral CT. (*a, d*) Thresholded outlines of the unfiltered PSF sections. (*b, e*) Unfiltered PSF. (*c, f*) Final filtered PSF. For $z < 0$ the results are antisymmetric.

3.2. Two-slice parallel-beam spiral CT

Consider two-slice parallel-beam spiral CT with pitch 4 (we define the pitch with respect to the width of *one* detector). Assuming that the input is an impulse located at the origin, the datasets acquired by the two detector arrays are (see equation 6):

$$g_1(s,\tau) = \delta(s)g_1(\tau) = \delta(s)\begin{cases} 1 & 0 \le \tau < \frac{\pi}{2} \\ 0 & \text{otherwise} \end{cases} \tag{22}$$

$$g_2(s,\tau) = \delta(s)g_2(\tau) = \delta(s)\begin{cases} 1 & -\frac{\pi}{2} \le \tau < 0 \\ 0 & \text{otherwise} \end{cases} \tag{23}$$

The estimated effective sinogram, according to equations 7 and 8, is

$$\bar{g}(s,\theta,z) = \delta(s)g_1(\theta)w((2\frac{\theta}{\pi} - \frac{1}{2})d - z) + \delta(s)g_2(\theta)w((2\frac{\theta}{\pi} + \frac{1}{2})d - z) \tag{24}$$

and the analytical equation for the unfiltered PSF is

$$b(r,\varphi,z) = \frac{1}{r}\begin{cases} g_1(\varphi + \frac{\pi}{2})w((2\frac{\varphi}{\pi} + \frac{1}{2})d - z) + g_2(\varphi + \frac{\pi}{2})w((2\frac{\varphi}{\pi} + \frac{3}{2})d - z) \\ \qquad\qquad -\pi \le \varphi < 0 \\ g_1(\varphi - \frac{\pi}{2})w((2\frac{\varphi}{\pi} - \frac{3}{2})d - z) + g_2(\varphi - \frac{\pi}{2})w((2\frac{\varphi}{\pi} - \frac{1}{2})d - z) \\ \qquad\qquad 0 \le \varphi < \pi \end{cases} \tag{25}$$

Sections through the 3-D PSF are shown in figure 2 (right).

3.3. Multi-slice parallel-beam spiral CT

One can show, similarly to the two-slice case described above, that for N-slice spiral CT with pitch $2N$, the unfiltered PSF is obtained by angular compression of the domain of the single-slice unfiltered PSF from 2π to $2\pi/N$, and N-fold replication. The resulting PSF will have $2N$ lobes. Note that if the pitch is $2k$, where k is an integer less than N, the traces of some of the detectors overlap, creating duplication of the data already acquired. This will result in k-fold compression and replication, and $2k$ lobes. For non-integer pitch values, the PSF may have more complicated shapes.

3.4. Single-slice fan-beam spiral CT

Consider a single-slice fan-beam spiral CT with pitch 2 and an impulse function input, located at $(x_0, y_0, 0)$, or $(r_0, \varphi_0, 0)$. According to (13),

$$g_{\text{fan}}(\beta,\gamma) = \delta(x_0\cos(\gamma+\beta) + y_0\sin(\gamma+\beta) - R\sin\gamma)\cdot \begin{cases} 1 & -\pi/2 \le \beta < \pi/2 \\ 0 & \text{otherwise} \end{cases} \tag{26}$$

The estimation of the effective planar dataset (14) reduces to

$$\begin{aligned} \bar{g}_{\text{fan}}(\alpha,\gamma,z) = {} & w(\alpha - \frac{z}{d}\pi,\gamma)\delta(x_0\cos(\gamma+\alpha) + y_0\sin(\gamma+\alpha) - R\sin\gamma) \\ & \cdot \begin{cases} 1 & -\pi/2 \le \alpha < \pi/2 \\ 0 & \text{otherwise} \end{cases} \end{aligned} \tag{27}$$

Substituting this into (16) yields

$$\begin{aligned} \bar{g}(s,\theta,z) = {} & w(\theta - a - \frac{z}{d}\pi, a)\delta(x_0\cos\theta + y_0\sin\theta - s)\cdot \begin{cases} 1 & -\frac{\pi}{2} \le \theta - a < \frac{\pi}{2} \\ 0 & \text{otherwise} \end{cases} \\ & + w([\theta + a + \pi]_{-\pi}^{\pi} - \frac{z}{d}\pi, -a)\delta(x_0\cos\theta + y_0\sin\theta - s) \\ & \cdot \begin{cases} 1 & -\frac{\pi}{2} \le [\theta + a + \pi]_{-\pi}^{\pi} < \frac{\pi}{2} \\ 0 & \text{otherwise} \end{cases} \end{aligned} \tag{28}$$

where $a \equiv \arcsin(s/R)$. Note that the δ function is non-zero only for $s = r_0\cos(\theta - \varphi_0)$. Therefore,

$$a = a(\theta) = \arcsin\frac{r_0\cos(\theta-\varphi_0)}{R}\ . \tag{29}$$

We now see that $\bar{g}(s,\theta,z)$ in (28) is of the special separable form (17), so we can obtain the analytical expression for the PSF using the Lemma (18).

Thresholded outlines of the unfiltered single-slice fan-beam PSFs, at five different locations, are shown in figure 3. The PSF at the isocenter (figure 3*a*) is identical to the PSF of *parallel-beam* spiral model (figure 2 left). The further the input impulse is from the isocenter, the more distorted (relative to its shape at the isocenter) the PSF becomes. The distortion type depends on the impulse location relative to the position of the x-ray source when it passes by the impulse. Different distortion types are shown in figure 3*b*-*e* assuming the x-ray source was at the "north" ($\beta = 0$).

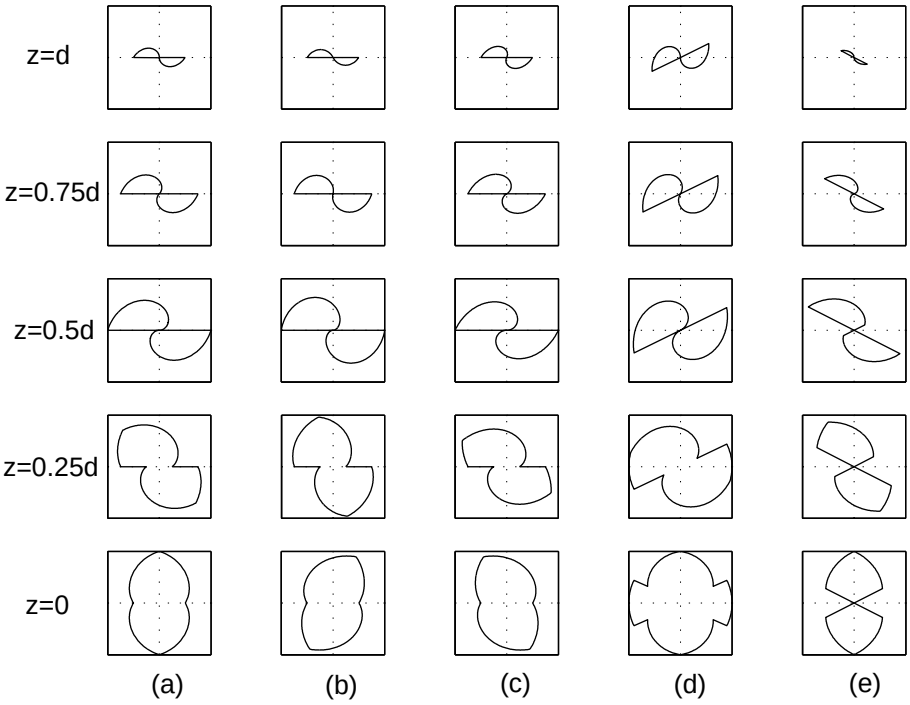

Figure 3. Thresholded outlines of the unfiltered PSF of fan beam spiral CT. The five columns correspond to different impulse locations in the $z = 0$ plane. *a:* $(0, 0)$. *b:* $(-R/2, 0)$. *c:* $(R/2, 0)$. *d:* $(0, R/2)$. *e:* $(0, -R/2)$. For $z < 0$ the PSF is antisymmetric.

When an impulse at the isocenter moves in z, the PSF rotates around the z axis, following the rotation of the x-ray source corresponding to the z shift of the impulse. When an impulse out of the isocenter moves in z, the PSF both rotates and changes its distortion type.

3.5. Multi-slice fan-beam spiral CT

The full analysis is omitted for brevity. It can be shown that for an impulse located at the isocenter the multi-slice fan-beam PSF is equal to the multi-slice parallel-beam PSF derived in sections 3.2 and 3.3. Near the isocenter they are nearly equal. For an impulse far from the isocenter, the shape of the PSF is distorted by the fan-beam effect, like in figure 3.

3.6. Cone-beam spiral CT

As we discussed in section 2.5, there are dozens of different cone-beam reconstruction algorithms. We have chosen to analyze the PSF of ASSR algorithm (Kachelrieß *et al* 2000) as a typical approximate algorithm that is probably in practical use.

In Appendix A we derive the PSF of the ASSR cone-beam reconstruction algorithm for an impulse located at the isocenter. The resulting PSF is identical to the PSF of multi-slice fan-beam and multi-slice parallel-beam geometries, described in the previous

sections. This is a remarkable result, indicating the fundamental nature of the PSF properties observed.

We believe that the PSF for other cone-beam algorithms should also share basic properties with the fan-beam PSF. The spatial variance in z is not due to a specific reconstruction technique, but to the discretization in z (finite width of the detectors) and helical rotation of the source. We can hardly expect that this variance can be fully compensated as part of the reconstruction process.

The spatial variance of the PSF can be regarded as a manifestation of aliasing. Indeed, scanned objects are not band-limited, and are not subjected to explicit anti-aliasing filtering before the longitudinal sampling by the detectors. Thus, undersampling and aliasing effects seem to be inherent. The lobes in the PSF appear to be a basic phenomenon as well. Reasonable reconstruction algorithms are likely to be biased towards input impulses that are precisely in level with a detector row, leading to lobes at regular angular intervals. Thus, the observed PSF properties should be common to a wide range of reconstruction algorithms.

4. Experimental Results

We carried out preliminary experiments, to demonstrate direct measurement of the PSF of a spiral CT system and to support the theoretical results.

We used tiny tin balls, of diameter 0.2mm, to approximate the delta functions. In a typical test, we placed two balls on top of a plastic box, near the isocenter. Their z coordinates differed by a fraction of a millimeter.

The experiments were performed with a Philips Brilliance 16-slice CT scanner, operated in 4-slice mode with pitch 2 (defined relative to *one* detector width). With this small pitch, the traces of all 4 detectors effectively overlap. Thus, according to our analysis, the PSF should be similar to that of a single-slice CT scanner with pitch 2 (see section 3.3). The scanner provides slices at 0.1mm intervals.

Figure 4 shows the balls as seen in three slices, about 0.3mm apart. Consider first the left ball. It appears in each slice roughly as an elongated shape, turning as the z coordinate is increased. The right ball also appears in the slices as a turning elongated shape, but due to its different z coordinate, the orientation of the shapes is different.

Figure 5 compares the shape orientations in sections of the PSF, as experimentally observed in slices, with those derived from the theoretically predicted PSF, for each of the two balls. The orientations were calculated using moment analysis. As we can see, in sections through the PSF of each ball, the shapes turn by almost 180 degrees as z varies along the PSF. There is a good match between the theoretical and experimental result in this crucial feature. This twist effect cannot be attributed to the metal artifact, which normally produces patterns rotating at the speed of x-ray source (Kachelrieß 1998), which is twice as fast as the observed in our experiment.

Note the vertical offset in the graphs that correspond to the two balls in figure 5. It reflects the spatial variance of the PSF, as predicted in our analysis. The 20 degrees

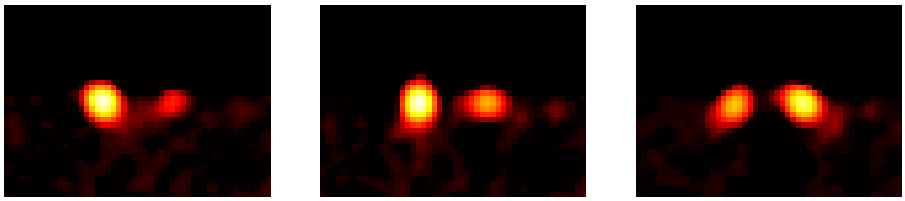

Figure 4. Three reconstructed slices, about 0.3mm apart, through the 3D spiral CT image of two tiny tin balls. The scanner was configured as a spiral single-detector machine. Each slice is a section through two 3D point spread functions. In each slice, the PSF appears as an elongated shape, turning as a function of z. This peculiar behavior is consistent with the analytic prediction.

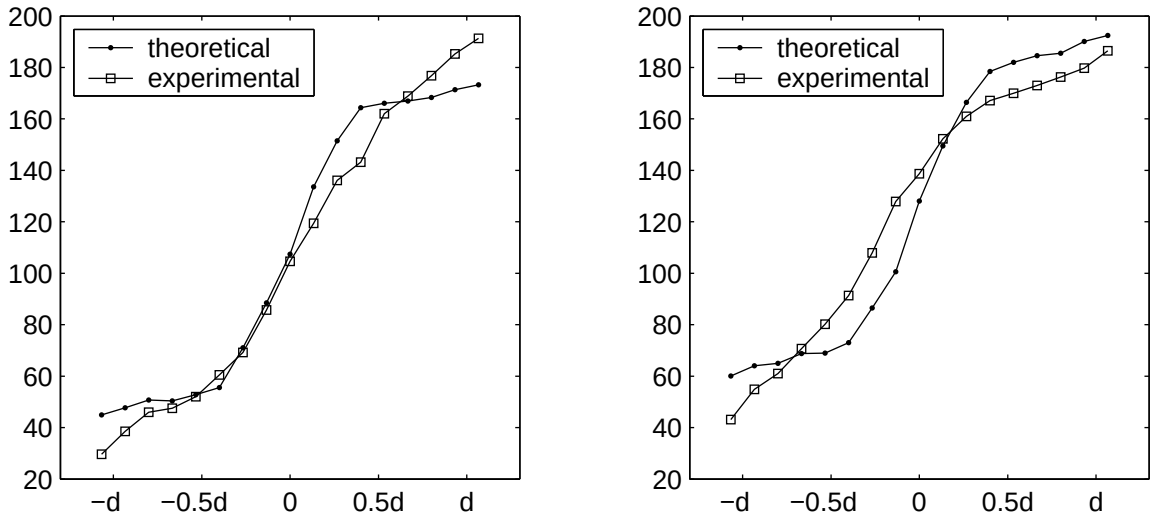

Figure 5. Comparison of the shape orientations in sections of the PSF, as experimentally observed in slices, with those derived from the theoretically predicted PSF. Orientation (in degrees) is presented as a function of the slice z-position. The left and right plots correspond to the left and right balls in figure 4.

relative orientation is in good agreement with the z-distance between them.

The eccentricity of the measured PSF sections is less than in the 180LI theoretical model. This is not surprising, due to several factors that we have not yet considered. First, the size of the measured ball (0.2mm) is small, but not infinitesimal relative to the detector width (0.75mm collimated, 1.5mm uncollimated) of our CT scanner. This means that we should account for the rotation of the X-ray source while it passes (in z) by the ball. It can be shown that the effect of this imperfect measurement can be approximated by 30 degrees rotational averaging of the theoretical PSF. Such averaging would preserve the orientation of the PSF section, but lower its eccentricity, just as we observe.

The second factor is the non-zero extent of the X-ray focal spot in z. It is equivalent to blurring the input image in z with a blur kernel of half the focal spot size. The effect

would be the same as that caused by the non-infinitesimal size of the target, that is, approximately, rotational averaging of the PSF.

Experimental results with a phantom containing small metallic balls have recently been reported by Meinel *et al* (2003). Focusing on spatial variation in the xy plane, irregularities in the observed shapes or spatial variation in z were not reported in that paper. The ball size of 0.8mm they used was too large relative to d, and could not approximate an impulse function. This must have lead to strong averaging of the PSF, making it nearly isotropic.

5. Conclusion

The 3D PSF of spiral CT systems does not resemble an isotropic Gaussian. Its shape depends on the specific configuration and on the reconstruction algorithm used. Spiral pasta, with its axis parallel to the z-axis of the scanner, can serve as a crude conceptual illustration of the types of shapes that the 3D PSF can assume.

Indirect measurements of the PSF, e.g. by imaging a thin wire parallel to the z-axis, or by analysis of step responses obtained at the surface of a large ball, can be misleading. In the case of the wire, an isotropic 2D "PSF" is measured due to the superposition of contributions from nearby layers. In the case of a large ball, the assumptions of separability and space invariance of the PSF do not hold and lead to inadequate estimation of the PSF.

The 3D PSF of a spiral CT system is generally asymmetric, non-separable and space variant. Manifestations of these phenomena have indeed been observed and analyzed in Wang and Vannier (1994b), Wang *et al* (1994), Yen *et al* (1999a,b), La Riviere and Pan (2002a), but have mostly been expressed in the context of spatial variation of the slice sensitivity profile, longitudinal sampling and longitudinal aliasing. Approaching these effects via the 3D PSF is direct and illuminating.

The complicated shape of the PSF is an undesirable phenomenon. The major disadvantage is not the space-variance in the xy plane, that has been considered in the past, but the anisotropy of the PSF shape combined with the rotational space-variance. Specifically, it can can distort small details, lead to stair-step and streaking artifacts, and create misleading differences between adjacent reconstructed slices.

This analysis calls for reconsideration of image quality assessment methods. Existing methodologies are based on two measures. One represents in-plane resolution, and can be associated with the average size of the PSF projected onto the xy plane. The second is the slice sensitivity profile, which represents the average PSF projected onto the z axis. Had the PSF been separable, these two measures would have provided a full description of the PSF and the image quality. However, they provide no information about the damaging anisotropy.

An isotropy measure should be introduced as the third important parameter of spiral CT image quality. One possible definition of an isotropy measure is the following. For each xy slice of the PSF, consider an isocurve at a certain threshold. Define the

isotropy of a slice as the ratio between the minimum and maximum distance of the isocurve from the origin. Thus, for an isotropic PSF the isocurve would be a circle, and the isotropy would be equal to 1. For all other shapes the values would be smaller. The isotropy of the entire PSF can be defined as a (possibly weighted) average of isotropy over all its slices. Note that the pitch can have a significant influence on the isotropy, and the CT operator must be aware of this fact.

Following the introduction of a new isotropy quality parameter, not only the reconstruction algorithms, but also other CT scanner design issues will have to be revisited. Isotropy improvement may have to be considered even at the expense of some degradation of the in-plane resolution and slice-sensitivity profile measures.

We observed that the anisotropy and rotational space-variance are manifestation of longitudinal aliasing, due to the longitudinal undersampling associated with the spiral data acquisition (section 3.6). However, as discussed in section 4, the non-zero z extent of the focal spot of the X-ray source is equivalent to blurring the input in z. Thus, the focal spot can serve as a natural (although not ideal) anti-aliasing filter. Currently, CT developers are motivated to make the spot as small as possible to improve the resolution and the SSP. One may consider to deliberately enlarge it in the z direction, to obtain anti-aliasing and thus improve the isotropy. The exact size could be tuned to balance between isotropy improvement and SSP degradation.

Another possible application of our results is in CT image deblurring. Successful deblurring has been reported (Wang *et al* 1995, Wang *et al* 1998, Jiang *et al* 2003). but in all these works a Gaussian PSF had been assumed. Having a more accurate PSF model can lead to better deblurring results.

A possible topic for future research is analysis of the PSF of various cone-beam algorithms, both approximate and exact, and comparative performance evaluation with respect to isotropy as well as the classical in-plane resolution and SSP measures.

Acknowledgments

We thank Dr. Gregory Volpe for his help in producing the experimental phantom, and Dr. Meir Faibel from the Sheba Medical Center for granting access to the CT scanner. This research was supported in part by the Ministry of Science and Technology.

Appendix A. The PSF of the ASSR cone-beam reconstruction algorithm

In this appendix we derive the PSF of cone-beam CT that uses the ASSR reconstruction algorithm, for an impulse located at the isocenter. The derivation is based on the description of the ASSR algorithm by Kachelrieß *et al* (2000). We assume that the reader is familiar with this work, and adopt its notations.

Consider a cone-beam CT system with a flat detector (u, v). The rotation radii of the source (R_F) and the detector (R_D) are equal. The focal spot of the source is

infinitesimally small. The detector consists of N_b slices of width $\bar{b}$ in the z-direction. The collimated width of a single detector (projected onto the isocenter) is

$$\Delta b = \frac{\bar{b}}{2} \ . \tag{A.1}$$

Let the pitch, defined relative to a *single* collimated slice width Δb, be equal to $2k$, where k is an integer. Let the object be

$$f(x, y, z) = \delta(x, y, z) \ . \tag{A.2}$$

The acquired dataset, denoted $p(\alpha, u, v)$, where α is a source position, is then

$$p(\alpha, u, v) = \delta(u)\delta(v + \frac{2k\Delta b}{\pi}\alpha) \ . \tag{A.3}$$

However, we must take into account discretization in the z axis, that is in v. The measurements are averaged over the detector width $\bar{b}$. During the reconstruction, these discrete values must be interpolated. Linear interpolation is proposed in (Kachelrieß *et al* 2000 section G). Then the interpolated dataset is

$$p_{\text{int}}(\alpha, u, v) = \delta(u) \begin{cases} \cdots & \\ \operatorname{tr}(v - \frac{3}{2}\bar{b}) & -2\frac{\pi}{k} \le \alpha < -\frac{\pi}{k} \\ \operatorname{tr}(v - \frac{1}{2}\bar{b}) & -\frac{\pi}{k} \le \alpha < 0 \\ \operatorname{tr}(v + \frac{1}{2}\bar{b}) & 0 \le \alpha < \frac{\pi}{k} \\ \operatorname{tr}(v + \frac{3}{2}\bar{b}) & \frac{\pi}{k} \le \alpha < 2\frac{\pi}{k} \\ \cdots & \end{cases} \tag{A.4}$$

where $\operatorname{tr}(x)$ is a triangular interpolation function with support $(-\bar{b}, \bar{b})$ and height 1. The number of terms is N_b.

We proceed with the reconstruction process described in section G, starting with choosing reconstruction positions α_R. The natural choice will be such that for each plane $z = z_0$ on the (x, y, z) reconstruction grid there will be one corresponding tilted reconstruction plane, so that they intersect at $(0, 0, z)$. Then

$$\alpha_R = \frac{\pi}{k\Delta b} z \tag{A.5}$$

Now let us reconstruct a parallel-beam dataset $p(\vartheta, \xi)$ for each $\vartheta \in [-\frac{1}{2}\pi, \frac{1}{2}\pi)$ and each ξ. The relative ray direction is

$$\alpha'_L(\vartheta, \xi) = \vartheta + \arcsin \frac{\xi}{R_F} \tag{A.6}$$

and the ray hit coordinates on the detector plane are

$$u_F(\vartheta, \xi, \alpha') = 2\xi / \sqrt{1 - (\xi/R_F)^2} \qquad v_F(\vartheta, \xi, \alpha') = -2k\Delta b\alpha'/\pi \tag{A.7}$$

The parallel-beam dataset $p(\vartheta, \xi)$ reconstructed from the interpolated measured dataset $p_{\text{int}}(\alpha, u, v)$ is

$$p(\vartheta, \xi) \approx p_{\text{int}} \left(\vartheta + \arcsin \frac{\xi}{R_F} + \frac{\pi z}{k\Delta b}, \frac{2\xi}{\sqrt{1 - (\frac{\xi}{R_F})^2}}, \frac{-2k\Delta b(\vartheta + \arcsin \frac{\xi}{R_F})}{\pi} \right) \tag{A.8}$$

Here we neglected two multiplicative correction terms, which are very close to 1. Substituting this into (A.4) gives for $z = 0$

$$p(\vartheta,\xi) = \frac{1}{2}\delta(\xi)\begin{cases} \cdots & \\ \mathrm{tr}(\bar{b}(-\frac{k\vartheta}{\pi}-\frac{1}{2})) & -\frac{\pi}{k} \le \vartheta < 0 \\ \mathrm{tr}(\bar{b}(-\frac{k\vartheta}{\pi}+\frac{1}{2})) & 0 \le \vartheta < \frac{\pi}{k} \\ \cdots & \end{cases} \tag{A.9}$$

where the number of terms is k, provided that $k \le N_b$, because $\vartheta \in [-\pi/2, \pi/2)$. Reconstructing this sinogram using the Lemma we obtain a "flower" with $2k$ lobes, identical to the PSF of multi-slice parallel-beam and fan-beam geometries described in section 3.3. The last reconstruction step - z-interpolation - can be neglected, because the reconstructed tilted plane intersects the horizontal one at the isocenter, so in the vicinity of the isocenter (where the PSF is located) they are very close.

References

Chen Z and Ning R 2004 Three dimensional point spread function measurement of cone-beam computed tomography system by iterative edge blurring algorithm *Phys. Med. Biol.* **49** 1865–80

Crawford C R and King K F 1990 Computed tomography scanning with simultaneous patient translation *Med. Phys.* **17** 967–82

Dawson P and Lees W R 2001 Multi-slice technology in computed tomography *Clinical Radiology* **56** 302–309

Fleischmann D, Rubin G D, Paik D S, Yen S Y, Hilfiker P R, Beaulieu C F and Napel S 2000 Helical stair-step artifacts in single-slice versus multi-slice CT *Radiology* **216** 185–96

Flohr T, Stierstorfer K, Bruder H, Simon J, Polacin A and Schaller S 2003 Image reconstruction and image quality evaluation for a 16-slice CT scanner *Med. Phys.* **30** 832–45

Grangeat P 1991 Mathematical framework of cone beam 3D reconstruction via the first derivative of the Radon transform (in *Mathematical Methods in Tomography, Lecture notes in Mathematics 1497* Springer Verlag, Berlin) 66–97

Hsieh J 2003 Analytical models for multi-slice helical CT performance parameters *Med. Phys.* **30** 169–78

Hu H and Fox S H 1996 The effect of helical pitch and beam collimation in the lesion contrast and slice profile in helical CT imaging *Med. Phys.* **23** 1943–54

Jain A K 1989 *Fundamentals of Digital Image Processing* (Prentice Hall) Ch. 10

Jiang M, Wang G, Skinner M W, Rubinstein J T and Vannier M W 2003 Blind deblurring of spiral CT images *IEEE Trans. Med. Imaging* **22** 837–45

Kachelrieß M 1998 Reduction of metal artifacts in x-ray computed tomography *PhD Thesis, Friedrich-Alexander Universität Erlangen-Nürnberg*

Kachelrieß M, Schaller S and Kalender W A 2000 Advanced single-slice rebinning in cone-beam spiral CT *Med. Phys.* **27** 754–72

Katsevich A 2002 Theoretically exact filtered backprojection-type inversion algorithm for spiral CT *SIAM J. Appl. Math.* **62** 2012–26

Katsevich A 2004 Improved exact FBP algorithm for spiral CT *Adv. Appl. Math.* **32** 681–97

La Rivière P J and Pan X 2002a Pitch dependence of longitudinal sampling and aliasing effects in multi-slice helical computed tomography (CT) *Phys. Med. Biol.* **47** 2797–810

La Rivière P J and Pan X 2002b Anti-aliasing weighting functions for single-slice helical CT *IEEE Trans. Med. Imaging* **21** 978–90

Meinel J F, Wang G, Jiang M, Frei T, Vannier M and Hoffman E 2003 Spatial variation of resolution and noise in multi-detector row spiral CT *Acad. Radiol.* **10** 607–13

Noo F, Defrise M and Clackdoyle R 1999 Single-slice rebinning method for helical cone-beam CT *Phys. Med. Biol.* **44** 561–70

Noo F and Heuscher D J 2002 Image reconstruction from cone-beam data on a circular short-scan (in *Medical Imaging 2002: Image Processing. SPIE Proceedings, Vol 4684*) 50-59

Polacin A, Kalender W A, Brink J and Vannier M 1993 Measurement of slice sensitivity profiles in spiral CT *Med. Phys.* **21** 133–40

Rattey P A and Lindgren A G 1981 Sampling the 2-D Radon transform *IEEE Trans. on Acoustics, Speech and Signal Processing* **29** 994–1002

Schaller S, Flohr T, Klingenbeck K, Krause J, Fuchs T and Kalender W A 2000 Spiral interpolation algorithm for multislice spiral CT–part I: theory *IEEE Trans. Med. Imaging* **19** 822–34

Stierstorfer K, Flohr T, Bruder H 2002 Segmented multiple plane restoration - a novel approximate reconstruction scheme for multi-slice spiral CT *Phys. Med. Biol.* **47** 2571–81

Wang G and Vannier M W 1994a Longitudinal resolution in volumetric x-ray computerized tomography - analytical comparison between conventional and helical computerized tomography *Med. Phys.* **21** 429–33

Wang G and Vannier M W 1994b Spatial variation of section sensitivity profile in spiral computed tomography *Med. Phys.* **21** 1491–97

Wang G, Brink J A and Vannier M W 1994 Theoretical FWTM values in helical CT *Med. Phys.* **21** 753–54

Wang G, Skinner M W, Vannier M W 1995 Temporal bone volumetric image deblurring in spiral computed tomography scanning *Acad. Radiol.* **2** 888–95

Wang G, Vannier M W, Skinner M W, Cavalcanti M G P and Harding G W 1998 Spiral CT image deblurring for cochlear implantation *IEEE Trans. Med. Imaging* **17** 251–61

Wang G and Lee S W 2003 Overview of cone-beam CT algorithms *http://dolphin.radiology.uiowa.edu/ge/Lib/GePDF/093-ctta-dc.doc*

Yen S Y, Rubin G D, Yan C H and Napel S 1999a Longitudinal sampling and aliasing in spiral CT *IEEE Trans. Med. Imaging* **18** 43–58

Yen S Y, Rubin G D and Napel S 1999b Spatially-varying longitudinal aliasing and resolution in spiral CT *Med. Phys.* **26** 2617–25

Zou Y and Pan X 2004 Exact image reconstruction on PI line from minimum data in helical cone-beam CT *Phys. Med. Biol.* **49** 941–59